Fluid-structure interaction of a flexible cantilever cylinder at low Reynolds numbers

Shayan Heydari [1,*] Neelesh A. Patankar,[2] Mitra J. Z. Hartmann,[2] and Rajeev K. Jaiman [1]
[1]*Department of Mechanical Engineering, University of British Columbia, Vancouver, British Columbia, Canada V6T 1Z4*
[2]*Department of Mechanical Engineering, Northwestern University, 2145 Sheridan Road, Evanston, Illinois 60208, USA*

(Received 16 May 2021; accepted 11 January 2022; published 7 February 2022)

We present a numerical study that investigates the fluid-structure interaction of a flexible cantilever cylinder with a uniform flow at low Reynolds numbers (Re). A fully coupled fluid-structure solver based on the three-dimensional Navier-Stokes equations and Euler-Bernoulli beam theory is employed to examine the coupled dynamics of the flexible cylinder. Of particular interest is to explore the possibility of flow-induced vibrations at laminar subcritical Re, i.e., no periodic vortex shedding, and assess the extent to which such a flexible cylindrical beam could sustain the vibrations at this Re regime. We find that when certain conditions are satisfied, the flexible cantilever cylinder experiences sustained vortex-induced vibrations (VIVs), with the frequency of the transverse oscillations matching the first-mode natural frequency of the cylinder. The range of the frequency match, known as the lock-in regime, is found to have a strong dependence on the Reynolds number Re, mass ratio m^*, and reduced velocity U^*. Unlike the steady wake behind a stationary rigid cylinder, the wake of the flexible cantilever cylinder is shown to become unstable at Reynolds numbers as low as $\mathrm{Re} = 22$ when system parameters are within the lock-in regime. A combined VIV-galloping type instability is suggested as the mechanism behind the sustained unsteadiness in the wake and large-amplitude vibrations of the cylinder at laminar subcritical Re. These findings attempt to generalize our understanding of flow-induced vibrations in flexible cantilever structures and have a relevance to the development of novel bio-inspired flow-sensing devices.

DOI: 10.1103/PhysRevFluids.7.024702

I. INTRODUCTION

Flow-induced vibrations (FIVs) are omnipresent and play a significant role in numerous fields such as marine/offshore, civil, biomedical, and aerospace engineering. Considerable research has been done in recent decades to characterize the underlying mechanism and explore the practical aspects of flow-induced vibrations in a wide range of domains, including vibration control [1–3], energy harvesting [4–8], and sensing [9,10] applications. In particular, the phenomenon of flow-induced vibration in bluff bodies has received much attention in the literature due to the complex vortex dynamics and nonlinear physics involved in the interaction of a bluff body with fluid flow. Within this context, the flow-induced vibration of an elastically mounted rigid cylinder has served as a prototypical model in many experimental and numerical studies [11]. It has been shown that asymmetric vortex shedding from the wake of an elastically mounted rigid cylinder exerts unsteady loads that could lead to large-amplitude vibrations in the cylinder. These vibrations are typically

*Corresponding author: sheydari@mail.ubc.ca

called vortex-induced vibrations (VIVs) and are characterized by a frequency match between the frequency of the periodic vortex shedding and vibration frequency of the cylinder [12,13].

When the natural frequency of a freely vibrating cylinder is close to the vortex-shedding frequency, the VIV phenomenon results in a complex evolution of the shedding frequency, which deviates from the Strouhal frequency of its stationary counterpart. In this frequency regime, the vortex formation locks on to the natural frequency of the cylinder, creating a strong coupling between the cylinder and fluid flow [12]. Several studies have shown that the maximum vibration amplitude of an elastically mounted rigid cylinder, with only one degree of freedom in the transverse direction, is $O(D)$ [14], where D is the cylinder diameter. Furthermore, the maximum vibration amplitude is known to be a function of fluid and structural parameters, including Reynolds number and mass-damping ratio [15], and has been shown to have a slightly higher value for two-degree-of-freedom cylinders [16]. Comprehensive reviews regarding the vortex-induced vibration of elastically mounted rigid cylinders can be found in Refs. [14,15,17–19].

More recently, several studies have focused on the dynamic response of flexible slender structures at high Reynolds numbers [20–22] to give new physical insight into the phenomenon of vortex-induced vibration in bluff bodies. Due to the complex interaction of nonlinear wake dynamics with numerous flexible modes, the vortex-induced vibration modeling and prediction poses serious challenges for flexible structures. For example, studies on long offshore/marine risers with pinned-pinned structural support have found that ocean currents excite several vibration modes and frequencies along the span of risers during VIVs [23–25]. From a short-term perspective, vortex-induced vibrations could amplify the drag force and exert large dynamic bending stresses on the structure. These dynamic stresses, in turn, could lead to fatigue failure in these types of flexible structures in the long term if not controlled properly [26]. In addition to pinned-pinned cylindrical risers, flexible cantilever cylinders could also experience vortex-induced vibrations. According to an experimental study on the VIV response of flexible cylinders in the laminar flow regime, the dynamics of a flexible cantilever cylinder is different from the dynamics of a flexible pinned-pinned riser during VIVs. A flexible pinned-pinned marine riser has been shown to vibrate at monotonically increasing frequencies with each eigenmode gradually growing in modal weight as the flow velocity is increased [27]. However, for a flexible cantilever cylinder, although higher modes are observed at higher velocities, the cylinder has been shown to oscillate with only one vibration eigenmode during VIVs [28]. In line with the works done in the field of vortex-induced vibrations, in our current work, we examine the dynamic response of a flexible cantilever cylinder at low Reynolds numbers to give new insight into the subject of flow-induced vibration in flexible slender structures.

Our interest in studying the dynamics of a flexible cantilever cylinder at low Reynolds numbers originates from the intriguing problem of sensing through whiskers in some mammals, such as rats and seals. Experimental studies on the mechanical response of isolated rat vibrissae (whiskers) to low-speed airflow have revealed that air currents of magnitude 0.5 to 5.6 m/s, typically found in natural environments, generate significant vibrissal motion that carries information about the direction and magnitude of airflow [29,30]. More interestingly, behavioral experiments have shown that rats use the information from their whiskers to localize the airflow sources [31]. Similar to rats, marine mammals such as harbor seals and sea lions have been shown to utilize their whiskers to locate and track their prey in dark and muddy environments [32]. Harbor seals and sea lions can sense minuscule hydrodynamic disturbances in water flows and follow a trail left behind in the wake of swimming fish. An experimental study on a model of a seal whisker has shown that a seal whisker in the wake of a stationary rigid cylinder undergoes wake-induced vibrations, with the frequency of the oscillations matching the shedding frequency of the upstream wake [33]. According to Refs. [33,34], the special morphology and unique structural design of a seal's whiskers helps mitigate flow-induced vibrations in uniform flow.

While there are some recent investigations to explain the interaction between the whiskers and vortex dynamics [35,36], the underlying mechanisms of the hydrodynamic information extraction from the whisker-vortex interaction and the mechanoreceptor response at the whiskers' base are not

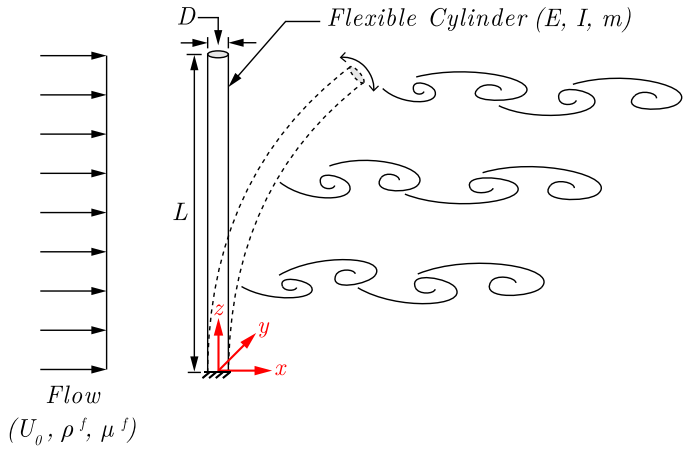

FIG. 1. Schematic of the flexible cantilever cylinder interacting with uniform flow.

systematically explored. Moreover, there exists neither a well-accepted hypothesis nor a computational modeling framework that explains the collective dynamics and vortex-sensing abilities via a whisker array. In particular, the oscillatory response of whiskers at laminar subcritical Reynolds numbers, i.e., $\mathrm{Re} < \mathrm{Re}_{\mathrm{cr}} \approx 45$ [37,38], is an area which requires further research. In our current work, we investigate the fluid-structure interaction of a flexible cantilever cylinder as a simplified whisker model using fully coupled numerical simulations. Our goal is to help answer two specific questions: (1) can we observe sustained vibrations in the flexible cantilever cylinder at laminar subcritical Re and (2) what is the relationship between the cylinder dynamics and stability of the wake at this Re regime? Understanding the underlying fluid-structure dynamics of a flexible cantilever cylinder, inspired by the dynamics of whiskers, is of vital importance for developing novel flow-measurement sensors [9] and brings us one step closer towards a complete mapping of the sensing properties of whiskers.

We model the whisker geometry as a cantilever cylinder with a constant circular cross-section and consider three key nondimensional parameters to examine the dynamics of the cylinder. The considered parameters are mass ratio m^*, Reynolds number Re, and reduced velocity U^* defined as

$$m^* = \frac{4m}{\pi D^2 \rho^{\mathrm{f}}}, \quad \mathrm{Re} = \frac{\rho^{\mathrm{f}} U_0 D}{\mu^{\mathrm{f}}}, \quad U^* = \frac{U_0}{f_{\mathrm{n}} D}, \tag{1}$$

where m is the mass per unit length of the cylinder, D is the cylinder diameter, ρ^{f} and μ^{f} are the density and dynamic viscosity of the fluid, respectively, U_0 is the magnitude of the uniform flow velocity, and f_{n} is the first-mode natural frequency of the cylinder. The range of the considered parameters in our current work is within $20 \leqslant \mathrm{Re} \leqslant 40$, $U^* \in [2, 19]$, and $1 \leqslant m^* \leqslant 1000$, which cover a practical range of values. A schematic of the flexible cantilever cylinder of length L is provided in Fig. 1. The cylinder is connected to a fixed support at $z = 0$. The Young's modulus and second moment of area of the cylinder are denoted by E and I, respectively. As shown in Fig. 1, due to fluid forces acting on the cylinder, it initially deforms in the streamwise direction. Furthermore, depending on the system parameters, the flexible cylinder could exhibit an unsteady dynamic response, with periodic vortex-shedding patterns present downstream.

The content of the paper is structured as follows. The governing equations for modeling the cylinder dynamics and the coupling strategy between the fluid and structural solvers are discussed in Sec. II. In addition, we provide the results for the grid convergence study at the end of this section. In Sec. III we cover the results of our study and discuss the dynamic response characteristics of the cylinder in detail. Finally, we finish the paper with a conclusion in Sec. IV.

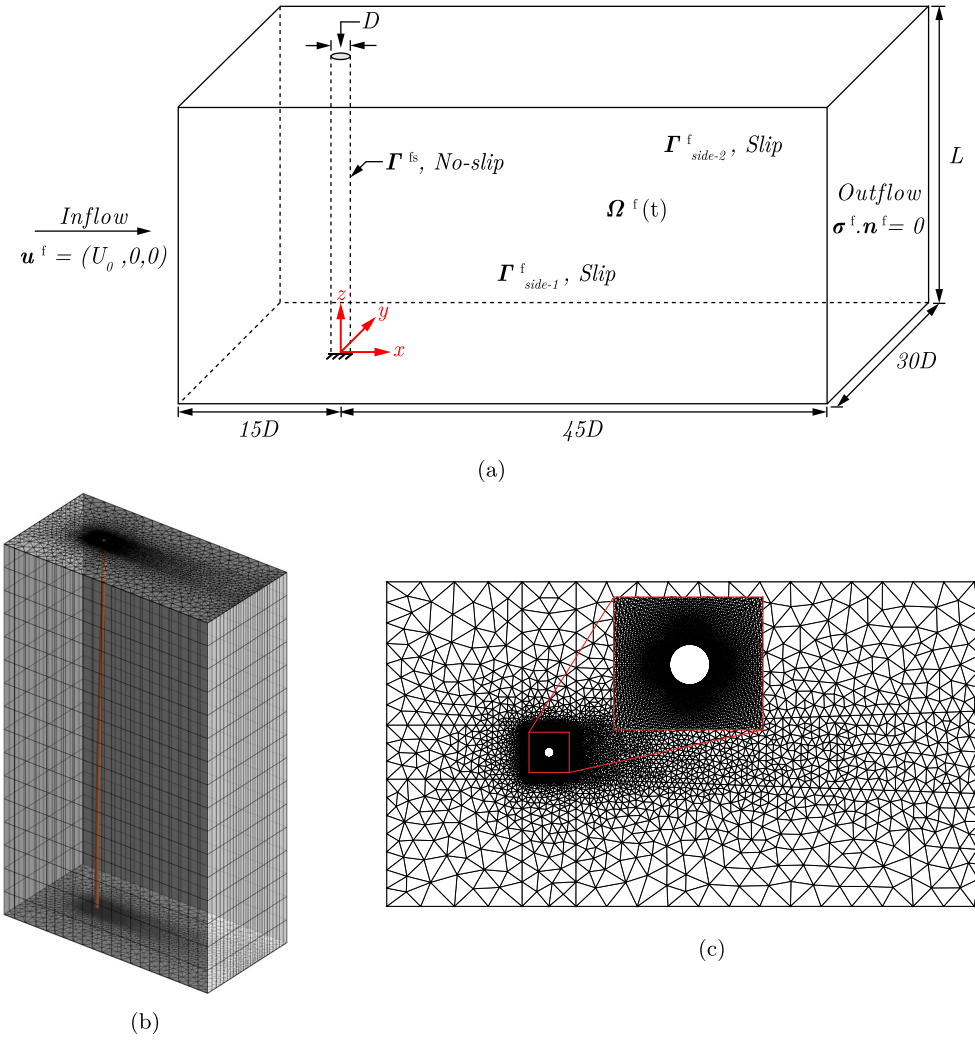

FIG. 2. (a) Schematic of the computational domain with details of the domain size and boundary conditions; (b) isometric view of the M2 mesh with the cylinder highlighted inside the domain; (c) representative z-plane slice of the unstructured finite element grid with a closeup view of the boundary layer mesh.

II. NUMERICAL METHODOLOGY

This section gives an overview of the employed numerical framework for modeling the fluid-structure interaction of the flexible cantilever cylinder. To model the cylinder dynamics, a three-dimensional computational domain, as shown in Fig. 2(a), is implemented. The cylinder is placed at an offset distance of $15D$ and $45D$ from the inflow and outflow surfaces, respectively. A fixed structural support condition is imposed at one end of the cylinder ($z = 0$), and the no-slip boundary condition is applied at the fluid-structure interface Γ^{fs}. The size of the computational domain is $60D \times 30D \times L$. A uniform flow of velocity $\boldsymbol{u}^{\mathrm{f}} = (U_0, 0, 0)$ is given at the inflow surface and the slip boundary condition is applied to the side surfaces $\boldsymbol{\Gamma}^{\mathrm{f}}_{side-1}$ and $\boldsymbol{\Gamma}^{\mathrm{f}}_{side-2}$. For the outflow surface, the traction-free boundary condition, given by $\boldsymbol{\sigma}^{\mathrm{f}} \cdot \boldsymbol{n}^{\mathrm{f}} = 0$, is specified.

The numerical framework has been extensively validated for the flow past a three-dimensional stationary circular cylinder and the flow past a long flexible cylinder under pinned-pinned structural

support at high Reynolds numbers with turbulent wake [24]. The validity of the framework in modeling the dynamics of flexible cylindrical structures enables us to accurately model the dynamics of the flexible cantilever cylinder in the presence of uniform flow at laminar subcritical Reynolds numbers, i.e., $\mathrm{Re} < \mathrm{Re}_{\mathrm{cr}} \approx 45$, in our current study. In the following, we present the governing equations for modeling the cylinder dynamics and discuss the implemented strategy for coupling the fluid and structural solvers. We also provide the grid convergence study results at the end of this section.

A. Governing equations

We consider the three-dimensional incompressible Navier-Stokes equations coupled with the Euler-Bernoulli beam theory to examine the coupled dynamics of the flexible cantilever cylinder. The governing equation for the Euler-Bernoulli beam is formulated in a Lagrangian reference frame, and a body-fitted moving boundary approach based on the arbitrary Lagrangian-Eulerian (ALE) description [39] is considered for the viscous incompressible fluid flow. The body-fitted treatment of the fluid-structure interface through the ALE description of the flow field enables us to accurately model the boundary layer over the deformable surface of the cylinder.

1. Navier-Stokes equations for a moving-boundary problem

The unsteady Navier-Stokes equations for a viscous incompressible fluid flow in an arbitrary Lagrangian-Eulerian reference frame on the fluid domain $\Omega^{\mathrm{f}}(t)$ are

$$\rho^{\mathrm{f}} \left.\frac{\partial \boldsymbol{u}^{\mathrm{f}}}{\partial t}\right|_{\hat{x}^{\mathrm{f}}} + \rho^{\mathrm{f}}(\boldsymbol{u}^{\mathrm{f}} - \boldsymbol{u}^{\mathrm{m}}) \cdot \boldsymbol{\nabla} \boldsymbol{u}^{\mathrm{f}} = \boldsymbol{\nabla} \cdot \boldsymbol{\sigma}^{\mathrm{f}} + \boldsymbol{b}^{\mathrm{f}} \quad \text{on} \quad \Omega^{\mathrm{f}}(t), \tag{2}$$

$$\boldsymbol{\nabla} \cdot \boldsymbol{u}^{\mathrm{f}} = 0 \quad \text{on} \quad \Omega^{\mathrm{f}}(t), \tag{3}$$

where $\boldsymbol{u}^{\mathrm{f}} = \boldsymbol{u}^{\mathrm{f}}(\boldsymbol{x}^{\mathrm{f}}, t)$ and $\boldsymbol{u}^{\mathrm{m}} = \boldsymbol{u}^{\mathrm{m}}(\boldsymbol{x}^{\mathrm{f}}, t)$ denote the fluid and mesh velocities defined for each spatial point $\boldsymbol{x}^{\mathrm{f}} \in \Omega^{\mathrm{f}}(t)$, respectively, $\boldsymbol{b}^{\mathrm{f}}$ is the body force applied to the fluid and $\boldsymbol{\sigma}^{\mathrm{f}}$ is the Cauchy stress tensor for a Newtonian fluid, given as

$$\boldsymbol{\sigma}^{\mathrm{f}} = -p\boldsymbol{I} + \mu^{\mathrm{f}}[\boldsymbol{\nabla} \boldsymbol{u}^{\mathrm{f}} + (\boldsymbol{\nabla} \boldsymbol{u}^{\mathrm{f}})^{T}], \tag{4}$$

where p denotes the fluid pressure, and μ^{f} is the dynamic viscosity of the fluid. The first term in Eq. (2) represents the partial derivative of $\boldsymbol{u}^{\mathrm{f}}$ with respect to time while the ALE referential coordinate $\hat{x}^{\mathrm{f}}$ is kept fixed.

The fluid forcing acting on the beam's surface is calculated by integrating the surface traction on the fluid-structure interface Γ^{fs}. The instantaneous coefficients of lift and drag forces are quantified as

$$C_{\mathrm{L}} = \frac{1}{\frac{1}{2}\rho^{\mathrm{f}} U_0^2 D L} \int_{\Gamma^{\mathrm{fs}}} (\boldsymbol{\sigma}^{\mathrm{f}} \cdot \boldsymbol{n}) \cdot \boldsymbol{n}_{\mathrm{y}} \, d\Gamma, \tag{5}$$

$$C_{\mathrm{D}} = \frac{1}{\frac{1}{2}\rho^{\mathrm{f}} U_0^2 D L} \int_{\Gamma^{\mathrm{fs}}} (\boldsymbol{\sigma}^{\mathrm{f}} \cdot \boldsymbol{n}) \cdot \boldsymbol{n}_{\mathrm{x}} \, d\Gamma, \tag{6}$$

where $\boldsymbol{n}_{\mathrm{x}}$ and $\boldsymbol{n}_{\mathrm{y}}$ are the Cartesian components of the unit outward normal vector $\boldsymbol{n}$.

2. Euler-Bernoulli beam theory for a flexible structure

We consider the flexible cantilever cylinder as a slender structure with relatively small lateral motions. Therefore, the Euler-Bernoulli beam theory can be applied to model its dynamic response. Let Ω^{s} be the structural domain consisting of structure coordinates $\boldsymbol{x}^{\mathrm{s}} = (x, y, z)$. We solve the transverse displacements $\boldsymbol{w}^{\mathrm{s}}(z, t)$ using the Euler-Bernoulli beam equation excited by the distributed unsteady fluid force per unit length $\boldsymbol{f}^{\mathrm{s}}$. The motion of the flexible cantilever cylinder is governed by the fluid forces and involves integrating pressure and shear stress effects on the cylinder surface.

TABLE I. Modal parameters for flexible cantilever beams of constant cross section [40].

Mode number, i	λ_i	σ_i
1	1.87510407	0.734095514
2	4.69409113	1.018467319
3	7.85475744	0.999224497
4	10.99554073	1.000033553
5	14.13716839	$\approx$1
$\geqslant 6$	$(2i-1)\pi/2$	$\approx$1

Neglecting the damping and shear effects, we take the equation of motion for the flexible cantilever cylinder as

$$m\frac{\partial^2 \boldsymbol{w}^{\mathrm{s}}(z,t)}{\partial t^2} + EI\frac{\partial^4 \boldsymbol{w}^{\mathrm{s}}(z,t)}{\partial z^4} = \boldsymbol{f}^{\mathrm{s}}(z,t), \tag{7}$$

where $m = \rho^{\mathrm{s}}A$ is the mass per unit length of the cylinder, with A being the cross-sectional area of the cylinder. Under the cantilever (clamped-free) configuration, the boundary conditions at the clamped end of the cylinder are given as

$$\boldsymbol{w}^{\mathrm{s}}(z,t)|_{z=0} = 0, \quad \left.\frac{\partial \boldsymbol{w}^{\mathrm{s}}(z,t)}{\partial z}\right|_{z=0} = 0. \tag{8}$$

To solve Eq. (7), we consider a mode superposition approach for the dynamic response of the cylinder. The ith mode natural frequency of the cylinder is given by

$$f_{\mathrm{n},i} = \frac{{\lambda_i}^2}{2\pi L^2}\sqrt{\frac{EI}{m+m_{\mathrm{a}}}}, \tag{9}$$

where i is the mode number, m_{a} is the added mass of the fluid per unit length defined as $m_{\mathrm{a}} = \pi D^2\rho^{\mathrm{f}}/4$, and λ_i is the dimensionless frequency parameter for the ith mode of vibration. The λ_i values are given in Table I. The modal parameters are based on the values reported in Ref. [40] for flexible cantilever beams of constant cross section.

The cylinder motion is solved using simple linear vibration analysis. The displacements from the mean position of the cylinder are assumed to be small and characterized based on the normal vibration modes found using an eigenvalue analysis. The mode shapes of the cantilever cylinder are taken as the sums of sine, cosine, sinh, and cosh functions of $\lambda_i z/L$ written as

$$S^i(z) = \cosh\left(\frac{\lambda_i z}{L}\right) - \cos\left(\frac{\lambda_i z}{L}\right) - \sigma_i \sinh\left(\frac{\lambda_i z}{L}\right) + \sigma_i \sin\left(\frac{\lambda_i z}{L}\right), \tag{10}$$

where S^i denotes the mode shape associated with the ith mode of vibration and σ_i is the nondimensional parameter dependent on the mode number (see Table I for σ_i values).

3. Treatment of the fluid-structure interface

We need to satisfy the continuity of velocity and traction at the fluid-structure interface. Let $\Gamma^{\mathrm{fs}} = \partial\Omega^{\mathrm{f}}(0) \cap \partial\Omega^{\mathrm{s}}$ be the fluid-structure interface at $t = 0$ and $\Gamma^{\mathrm{fs}}(t) = \boldsymbol{\varphi}^{\mathrm{s}}(\Gamma^{\mathrm{fs}}, t)$ be the interface at time t. The required conditions to be satisfied are

$$\boldsymbol{u}^{\mathrm{f}}(\boldsymbol{\varphi}^{\mathrm{s}}(\boldsymbol{x}_0^{\mathrm{s}}, t), t) = \boldsymbol{u}^{\mathrm{s}}(\boldsymbol{x}_0^{\mathrm{s}}, t), \tag{11}$$

$$\int_{\boldsymbol{\varphi}^{\mathrm{s}}(\gamma,t)} \boldsymbol{\sigma}^{\mathrm{f}}(\boldsymbol{x}^{\mathrm{f}}, t)\cdot\boldsymbol{n}\, d\Gamma(\boldsymbol{x}^{\mathrm{f}}) + \int_{\gamma} \boldsymbol{t}^{\mathrm{s}}\, d\Gamma = 0, \tag{12}$$

TABLE II. Grid convergence study results for the flexible cantilever cylinder at Re = 40, $m^* = 1$, and $U^* = 11$. The values inside the parentheses represent the relative error compared to the results of the M3 mesh. A constant time-step size $\Delta t = 0.001$ is employed.

	M1	M2	M3
Number of nodes	142 290	285 396	564 672
Number of elements	271 458	547 470	1 086 591
Frequency ratio f_y/f_n	1.2522	1.2522	1.2522
Mean streamwise deformation $\overline{A_x}/D$	2.6000 (0.26%)	2.5966 (0.13%)	2.5933
rms of transverse vibration amplitude A_y^{rms}/D	0.3188 (1.98%)	0.3134 (0.25%)	0.3126
Mean drag coefficient $\overline{C_D}$	1.6958 (0.37%)	1.6917 (0.13%)	1.6895
rms of lift coefficient C_L^{rms}	0.0197 (14.53%)	0.0175 (1.74%)	0.0172

where $\boldsymbol{\varphi}^s$ denotes the position vector that maps the initial position $\boldsymbol{x}_0^s$ of the cylinder to its position at time t, i.e., $\boldsymbol{\varphi}^s(\boldsymbol{x}^s, t) = \boldsymbol{x}_0^s + \boldsymbol{w}^s(\boldsymbol{x}^s, t)$, $\boldsymbol{t}^s$ is the fluid traction vector relating to the fluid forcing as $\boldsymbol{f}^s(z,t) = \int_{\Gamma^{fs}} \boldsymbol{t}^s \, d\Gamma$, and $\boldsymbol{u}^s$ is the velocity of the structure at time t given by $\boldsymbol{u}^s = \partial\boldsymbol{\varphi}^s/\partial t$. Here $\boldsymbol{n}$ is the outer normal to the fluid-structure interface, γ is any part of the interface Γ^{fs} in the reference configuration, $d\Gamma$ is the differential surface area and $\boldsymbol{\varphi}^s(\gamma, t)$ is the corresponding fluid part at time t. The above conditions are satisfied such that the fluid velocity is exactly equal to the velocity of the structure at the fluid-structure interface.

To couple the fluid and structure equations, we use a nonlinear partitioned iterative approach based on the nonlinear iterative force correction (NIFC) scheme described in Refs. [41,42]. At each time step, the fluid traction applied to the surface of the cylinder is projected onto the eigenvectors to find the values of the generalized modal forces. The projected modal forces are then used to determine the modal amplitudes and displacements for the next time step. To account for the changes in the cylinder geometry, we explicitly control the motion of each mesh node while satisfying the kinematic consistency of the discretized interface. The movement of the internal finite element nodes is chosen such that the mesh quality does not deteriorate as the displacements of the cylinder become large. For this purpose, we assume the fluid mesh to represent a hyperelastic solid model. In addition, a standard Lagrangian finite element technique is used to adapt the mesh to the new geometry of the domain.

B. Grid convergence study

This subsection provides the grid convergence study results for the flexible cantilever cylinder interacting with a uniform flow. The computational domain, shown in Fig. 2(a), is discretized into unstructured hexahedral finite element grids with a boundary layer mesh around the cylinder. We start with a relatively coarse grid denoted by M1 and successively increase the number of elements by approximately a factor of 2 to achieve the M2 and M3 meshes. An isometric view of the discretized domain and a z-plane slice of the unstructured grid for the M2 mesh is given in Figs. 2(b) and 2(c), respectively. For the grid convergence study, the response characteristics of the cylinder are examined at Re = 40, $m^* = 1$, and $U^* = 11$. Grid convergence errors are then calculated by taking the results for the finest mesh, M3, as the reference case. The values of the frequency ratio (f_y/f_n), mean streamwise deformation ($\overline{A_x}/D$), root-mean square (rms) of the dimensionless transverse vibration amplitude (A_y^{rms}/D), and the force coefficients ($\overline{C_D}$ and C_L^{rms}) are given in Table II. According to Table II, the relative errors using the M2 mesh are less than 2%; therefore, the M2 mesh is chosen as the suitable grid for our present study. It is worth noting that the results in Table II are for a computational domain consisting of 16 layers in the spanwise direction. After performing an independent grid convergence study on the number of spanwise layers, ranging from 8 to 64, the grid with 16 layers is found to capture the essential three-dimensional features of the fluid-structure system.

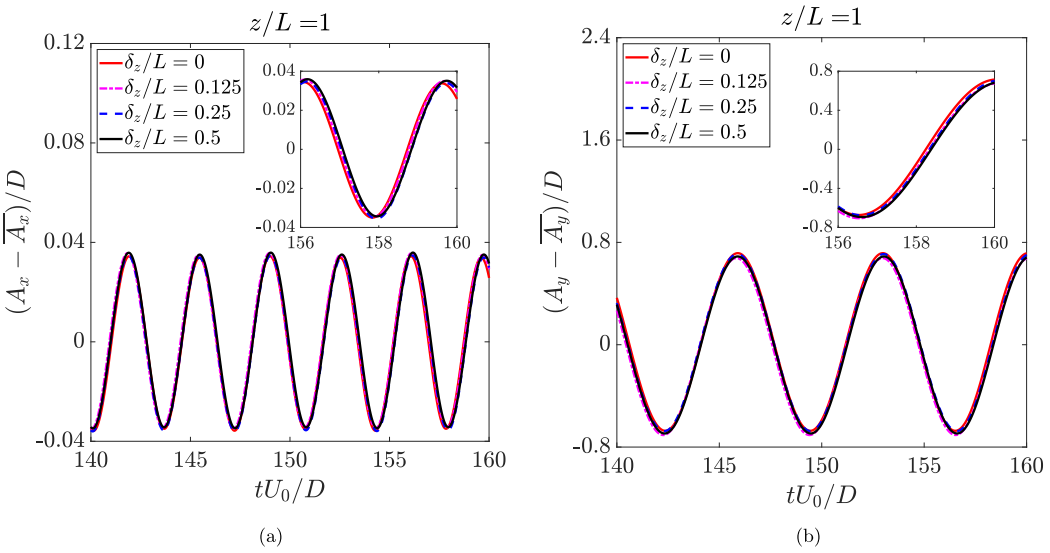

FIG. 3. Variations of the dimensionless (a) streamwise and (b) transverse vibration amplitude calculated from the mean deformed position of the cylinder at Re = 40, $m^* = 1$, and $U^* = 7$ in the time window $tU_0/D \in [140, 160]$. The results are probed at $z/L = 1$ for gap ratios ranging from $\delta_z/L = 0$ (no gap) to $\delta_z/L = 0.5$.

Next, the effect of the gap ratio on the oscillatory response of the cylinder is examined. The gap ratio is defined as δ_z/L where δ_z is the distance from the free end of the cylinder to the top surface of the domain. Figure 3 shows the amplitude response results for the flexible cantilever cylinder at Re = 40, $m^* = 1$, and $U^* = 7$ for the gap ratios in $\delta_z/L \in [0, 0.5]$. It is found that the gap ratio has a negligible effect on the cylinder response. The vortical structures around the free end of the cylinder for the domain with $\delta_z/L = 0.5$ are shown in Fig. 4. It is observed that the vortices are predominantly in the xy-plane near the free end of the cylinder. Table III provides a summary of the response characteristics of the cylinder and hydrodynamic coefficients for the range of studied gap ratios. We observe that the relative errors for $\delta_z/L = 0$, 0.125, and 0.25 are less than 2%, compared to $\delta_z/L = 0.5$. Moreover, no specific trend in the value of the relative errors is observed as the gap ratio is increased. For this particular problem, we conclude that the gap ratio effects are not significant, and the M2 mesh with no gap between the top surface of the domain and the free end of the cylinder can provide an adequate solution.

III. RESULTS AND DISCUSSION

A. Response characteristics

We first explore the response characteristics of the flexible cantilever cylinder of aspect ratio $L/D = 100$ for $20 \leqslant \mathrm{Re} \leqslant 40$, $U^* \in [2, 19]$, and $m^* = 1$. We investigate the response charac-

TABLE III. Results for the effect of gap ratio on the dynamics of the flexible cantilever cylinder at Re = 40, $m^* = 1$, and $U^* = 7$. The values inside the parentheses represent the relative error compared to the results of the domain with $\delta_z/L = 0.5$. A constant time-step size $\Delta t = 0.001$ is employed.

	$\delta_z/L = 0$	$\delta_z/L = 0.125$	$\delta_z/L = 0.25$	$\delta_z/L = 0.5$
Mean streamwise deformation $\overline{A_x}/D$	1.1956 (0.61%)	1.1896 (0.10%)	1.1899 (0.13%)	1.1884
rms of transverse vibration amplitude A_y^{rms}/D	0.4937 (1.86%)	0.4902 (1.13%)	0.4923 (1.57%)	0.4847
Mean drag coefficient $\overline{C_D}$	1.8714 (1.07%)	1.8531 (0.08%)	1.8514 (0.01%)	1.8516
rms of lift coefficient C_L^{rms}	0.3034 (1.44%)	0.3013 (0.73%)	0.3038 (1.57%)	0.2991

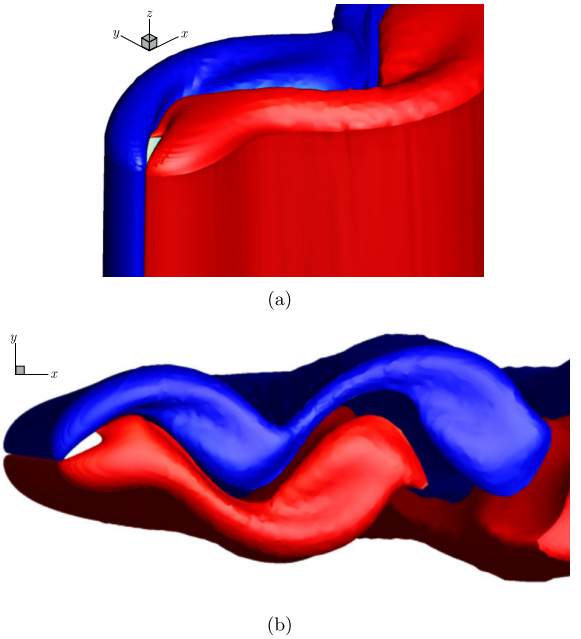

FIG. 4. (a) Isometric and (b) xy-plane view of the vortical structures visualized by the normalized z-vorticity isosurfaces ($\omega_z D/U_0 = -0.224, 0.224$) around the flexible cantilever cylinder at Re $= 40$, $m^* = 1$, and $U^* = 7$. The domain has a gap ratio $\delta_z/L = 0.5$. Red (blue) indicates regions of positive (negative) vortices.

teristics of the flexible cantilever cylinder in terms of the root-mean-square (rms) value of the dimensionless transverse vibration amplitude A_{y}^{rms}/D. As shown in Fig. 5, at Re $= 20$, the cylinder remains in its steady deflected position, i.e., $A_{\mathrm{y}}^{rms}/D = 0$, for the range of studied U^*. Similarly, this steady-state response is observed at Re $= 22$ for $U^* \leqslant 6$ and between $24 \leqslant$ Re $\leqslant 40$ for $U^* \leqslant 5$ (see Fig. 5). Although the flexible cantilever cylinder exhibits a steady-state response for some values of U^*, there is a particular range of U^* within which the cylinder undergoes sustained

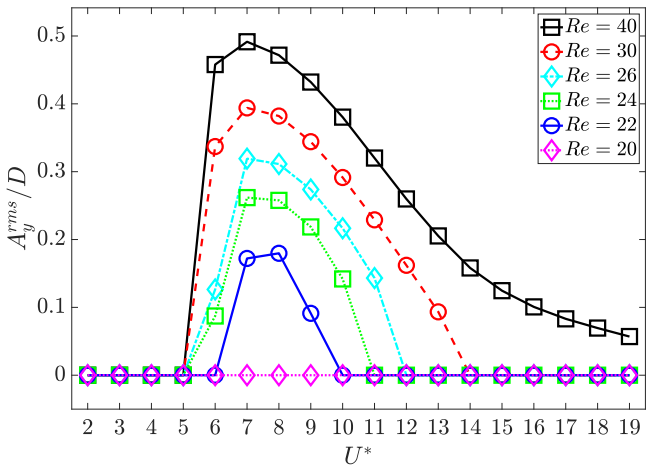

FIG. 5. Root-mean-square (rms) value of the dimensionless transverse vibration amplitude A_{y}^{rms}/D at $z/L = 1$ as a function of U^* at $m^* = 1$ for $20 \leqslant$ Re $\leqslant 40$.

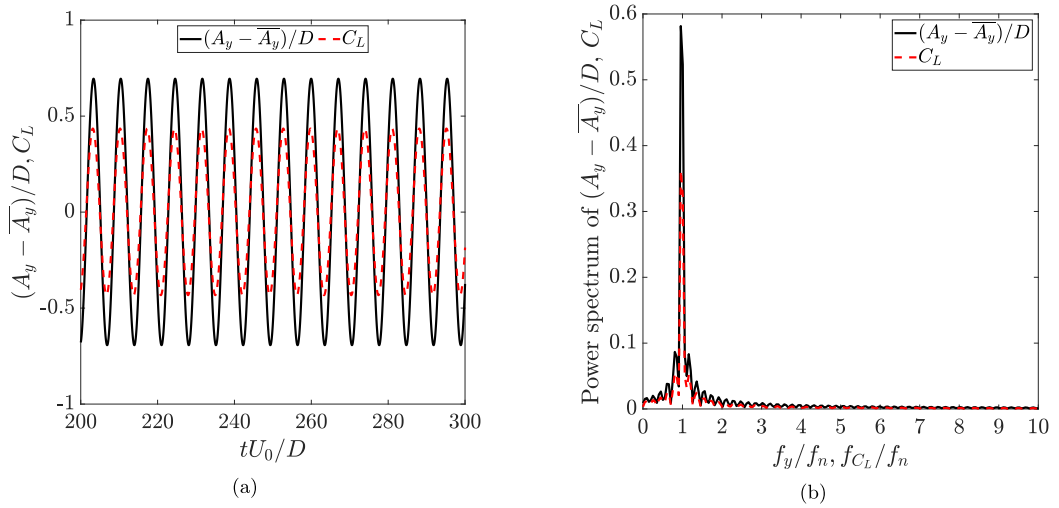

FIG. 6. (a) Variations of dimensionless transverse vibration amplitude calculated from the mean deformed position of the cylinder $(A_y - \overline{A_y})/D$, probed at $z/L = 1$, and the lift coefficient C_L in the time domain; (b) power spectra of $(A_y - \overline{A_y})/D$ and C_L in the frequency domain. The results are gathered in the time window $tU_0/D \in [200, 300]$ at Re $= 40$, $m^* = 1$, and $U^* = 7$.

large-amplitude vibrations. The peak of the transverse vibration amplitude in this range is shown to be within $U^* \in [7, 8]$ for Re $\geqslant 22$. According to Fig. 5, the peak of A_y^{rms}/D at Re $= 22$ is at $U^* = 8$ with a value of $A_y^{rms}/D \approx 0.18$. However, as Re is increased, the maximum value of the transverse vibration amplitude is found to increase in magnitude and shift towards $U^* = 7$. For instance, the peak of A_y^{rms}/D has a magnitude of approximately $A_y^{rms}/D \approx 0.26$ at Re $= 24$, increasing to $A_y^{rms}/D \approx 0.49$ at Re $= 40$. At Re $= 40$, the cylinder is shown to experience sustained vibrations for reduced velocities between $U^* \in [6, 19]$; however, for lower Reynolds numbers, the oscillations are present for a narrower range of U^*. A more broadband oscillatory response at higher Reynolds numbers is mainly due to larger inertial fluid forces that overcome the viscous damping effects.

Time histories of the transverse vibration amplitude calculated from the mean deformed position of the cylinder $(A_y - \overline{A_y})/D$ at $z/L = 1$ and the lift coefficient C_L are given in Fig. 6(a). We observe that the cylinder response in the transverse direction is in-phase with the variations of the lift coefficient at Re $= 40$, $m^* = 1$, and $U^* = 7$. Moreover, the peak of the dimensionless transverse vibration frequency f_y/f_n is shown to match the peak of the dimensionless lift coefficient frequency f_{C_L}/f_n in the frequency domain at $f_y/f_n = f_{C_L}/f_n = 1$ [see Fig. 6(b)]. This frequency match indicates the presence of the lock-in phenomenon at $U^* = 7$. We consider the lock-in regime as a region wherein $0.9 \leqslant f_{y,C_L}/f_n \leqslant 1.1$. To specify the range of the lock-in regime with respect to U^*, we have provided the variations of the dimensionless transverse vibration frequency f_y/f_n and the dimensionless lift coefficient frequency f_{C_L}/f_n at $m^* = 1$ for Re $= 22$, 30, and 40 in Fig. 7. According to Fig. 7, at Re $= 22$, the cylinder is in the lock-in regime for $U^* \in [8, 9]$, extending to $U^* \in [7, 10]$ at Re $= 30$ and to $U^* \in [6, 9]$ at Re $= 40$.

Figure 8 represents the variations of the cross-sectional drag and lift coefficients, given by C_d and C_l, respectively, in the time domain, along with the power spectra of the force and amplitude coefficients in the frequency domain, at Re $= 40$, $m^* = 1$, and $U^* = 7$. As shown in Fig. 8(a), the drag coefficient varies in time and across the cylinder span. We find that the mean value of the cross-sectional drag coefficient is $\overline{C_d} \approx 2.31$ at $z/L = 1$; however, this value is found to reduce to $\overline{C_d} \approx 1.57$ at $z = 0$. For a stationary rigid cylinder interacting with a uniform cross-flow at Re $= 40$, the drag coefficient has a uniform distribution along the cylinder span, with a value of $C_d \approx 1.55$ [43]; however, for the flexible cantilever cylinder at the same Re, the value of the fluctuating drag

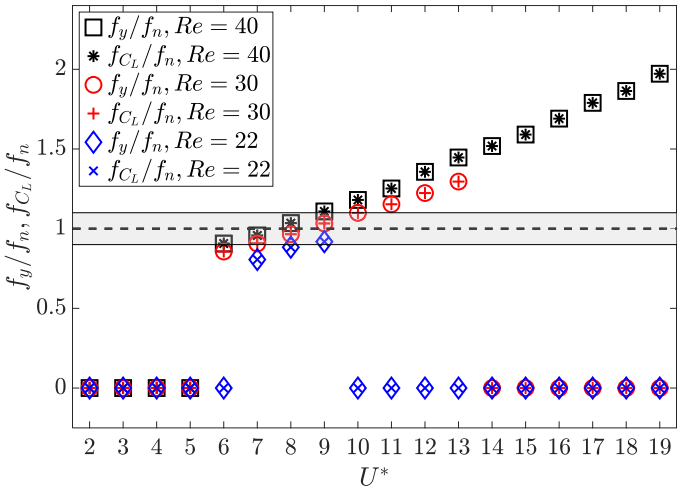

FIG. 7. Variations of the dimensionless transverse vibration frequency f_y/f_n, probed at $z/L = 1$, and the dimensionless lift coefficient frequency f_{C_L}/f_n with respect to U^*. The results are gathered at $m^* = 1$ for Re $= 22,\ 30$, and 40.

coefficient is shown to vary along the length of the cylinder. Although the magnitude of C_d increases by moving towards the free end of the cylinder, the magnitude of the fluctuating cross-sectional drag coefficient $C_d - \overline{C_d}$ reaches near zero at $z/L \approx 0.6$ [see Fig. 8(b)]. Nevertheless, the magnitude of the dimensionless streamwise vibration amplitude calculated from the mean deformed position of the cylinder $(A_x - \overline{A_x})/D$ is shown to increase monotonically moving from the fixed end to the free end of the cylinder. The variation of the cross-sectional lift coefficient across the cylinder span is shown in Fig. 8(c). We observe that the unsteady lift coefficient has a single frequency with a ratio of $f_{C_l}/f_n = 1$ across the length of the cylinder. Similar to the magnitude of the streamwise vibrations, the magnitude of the transverse vibrations is found to monotonically increase by moving from the fixed end to the free end of the cylinder [see Fig. 8(d)].

An isometric view of the cylinder undergoing large-amplitude oscillations in the lock-in regime at Re $= 40$, $m^* = 1$, and $U^* = 7$ is illustrated in Fig. 9(a). A figure-eight-shape motion trajectory is observed across the cylinder length. These trajectories are shown to grow in magnitude by moving towards the free end of the cylinder. The scalograms of the dynamic response of the cylinder in the streamwise and transverse directions, given in Figs. 9(b) and 9(c), respectively, suggest standing wave patterns in both the streamwise and transverse directions. Based on the scalograms of the cylinder given in Fig. 9 and the power spectra of the force and amplitude coefficients provided in Figs. 8(b) and 8(d), the dimensionless streamwise vibration frequency f_x/f_n is twice that of the dimensionless transverse vibration frequency f_y/f_n along the cylinder span. The frequency ratio of $f_x/f_y = 2$ explains the figure-eight-shape motion trajectory of the cylinder shown in Fig. 9(a). Finally, we have provided the motion trajectories of the free end of the cylinder at Re $= 40$, and $m^* = 1$ for $U^* \in [6, 9]$ in Fig. 10. A figure-eight-shape motion trajectory is observed for all values of U^* in the lock-in regime.

Next, we explore the power transfer between the fluid flow and the vibrating cantilever cylinder. Figure 11 shows a time history of the instantaneous power transfer from the fluid flow to the flexible cantilever cylinder in one period of the cylinder motion, i.e., $T = 1/f_n$. The dimensionless power transfer coefficients in the streamwise and transverse direction are defined as $(C_d - \overline{C_d})u/U_0$ and $(C_l - \overline{C_l})v/U_0$, respectively. Here $\overline{C_d}$ and $\overline{C_l}$ represent the mean value of the cross-sectional drag and lift coefficients, while u and v are the cross-sectional streamwise and cross-flow velocity of the cylinder, respectively. A complex interaction between the flexible cantilever cylinder and the wake

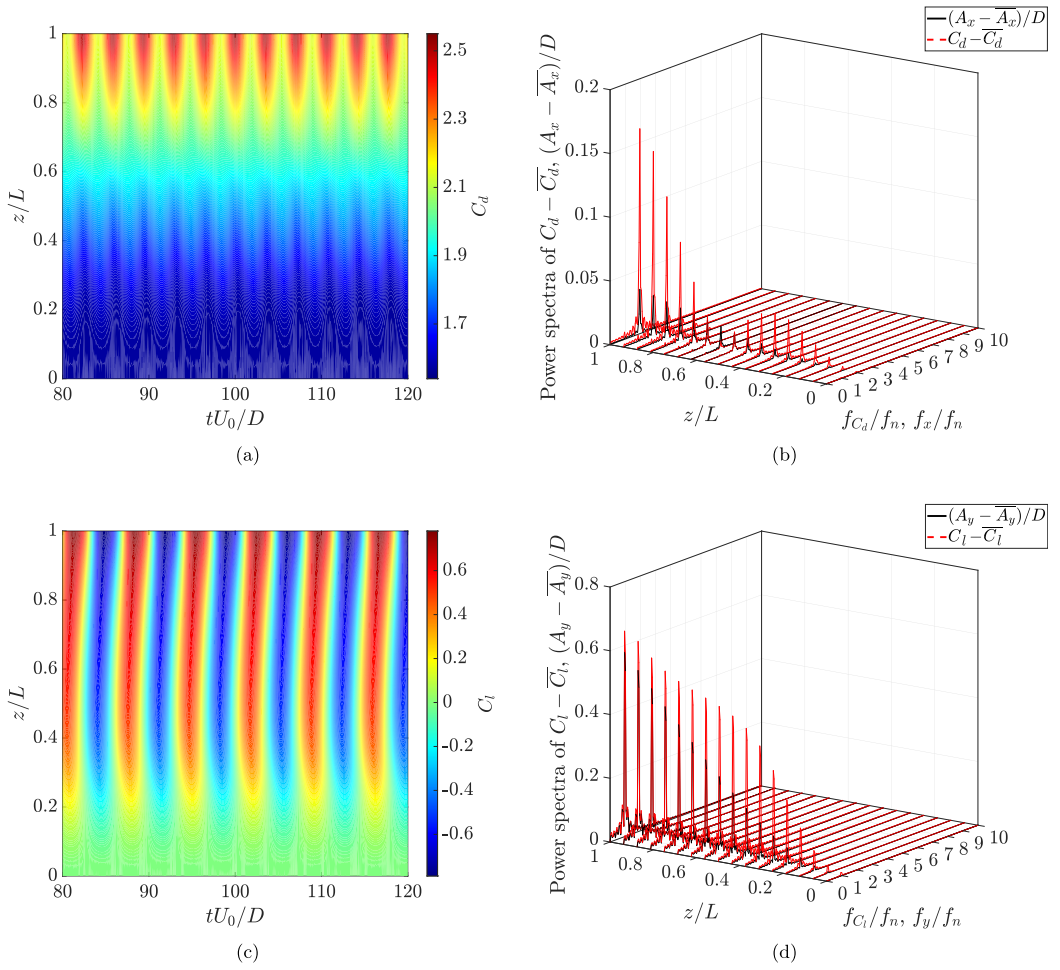

FIG. 8. (a) Variation of the cross-sectional drag coefficient C_d along the cylinder span in the time domain; (b) power spectra of $(A_\mathrm{x} - \overline{A_\mathrm{x}})/D$ and $C_\mathrm{d} - \overline{C_\mathrm{d}}$ in the frequency domain. (c) Variation of the cross-sectional lift coefficient C_l along the cylinder span in the time domain; (d) power spectra of $(A_\mathrm{y} - \overline{A_\mathrm{y}})/D$ and $C_\mathrm{l} - \overline{C_\mathrm{l}}$ in the frequency domain. The results are gathered in the time window $tU_0/D \in [80, 120]$ at $\mathrm{Re} = 40$, $m^* = 1$, and $U^* = 7$.

dynamics due to the spatial-temporal variations of fluid forces is shown to result in a cyclic power transfer in and out of the cylinder. Knowing the fluid forces and vibration response of the cylinder, the hydrodynamic coefficients in-phase with the cylinder velocity are obtained using the following equations:

$$C_\mathrm{du}(z) = \frac{\frac{2}{T}\int_T [C_\mathrm{d}(z,t) - \overline{C_\mathrm{d}}(z)]u(z,t)\,dt}{\sqrt{\frac{2}{T}\int_T u(z,t)^2 dt}}, \tag{13}$$

$$C_\mathrm{lv}(z) = \frac{\frac{2}{T}\int_T [C_\mathrm{l}(z,t) - \overline{C_\mathrm{l}}(z)]v(z,t)\,dt}{\sqrt{\frac{2}{T}\int_T v(z,t)^2\,dt}}, \tag{14}$$

where C_du and C_lv represent the hydrodynamic coefficients in-phase with the streamwise and cross-flow velocity of the cylinder, respectively. Figure 12 illustrates the distribution of C_du and C_lv

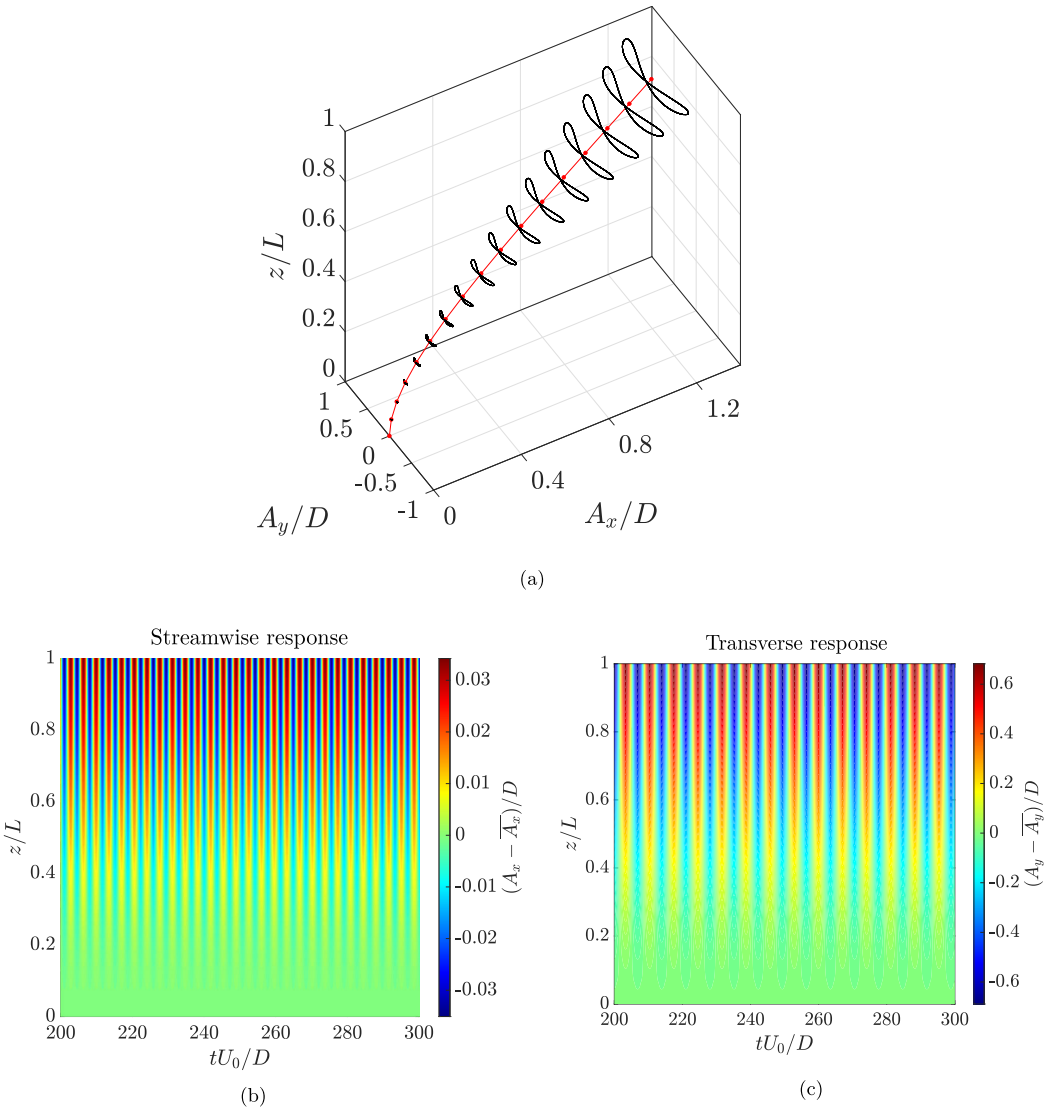

FIG. 9. (a) Motion trajectory of the flexible cantilever cylinder (illustrated by black lines); the red filled dots represent the mean position of the cylinder nodes and the red line corresponds to the cylinder's steady deflected position. (b) Scalogram of the vibrations in the streamwise direction. (c) Scalogram of the vibrations in the transverse direction. The results are gathered at Re = 40, $m^* = 1$, and $U^* = 7$ in the time window $tU_0/D \in [200, 300]$.

along the cylinder span at Re = 40, $m^* = 1$, and $U^* = 7$. We assume that $C_{\mathrm{du}} = C_{\mathrm{lv}} = 0$ at $z/L = 0$. According to Fig. 12, over one period of the cylinder motion, C_{lv} is positive within $z/L \in (0, 0.8)$ and negative in $z/L \in (0.8, 1)$. The positive values of the hydrodynamic coefficients indicate a positive net work done by the fluid flow on the cylinder in each direction, while the negative values are interpreted vice versa. As shown in Fig. 12, the magnitude of C_{du} varies less significantly along the cylinder span compared to the magnitude of C_{lv}. In addition, C_{du} is shown to have positive values approximately between $z/L \in (0.5, 0.85)$ and negative values elsewhere. Based on the values

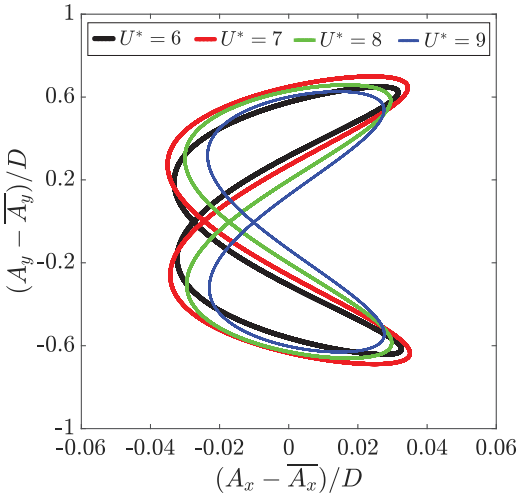

FIG. 10. Motion trajectory of the flexible cantilever cylinder probed at $z/L = 1$ for $\mathrm{Re} = 40$, $m^* = 1$, and $U^* \in [6, 9]$.

provided in Fig. 12, we can associate the self-sustained vibrations of the cylinder with the positive values of C_{lv} over $z/L \in (0, 0.8)$.

B. Wake dynamics during lock-in

A comparison between the wake of a stationary rigid cylinder, and the wake of the flexible cantilever cylinder at $z/L = 0.5$, $\mathrm{Re} = 40$, $m^* = 1$, and $U^* = 7$ is given in Fig. 13. We show that the wake of the stationary rigid cylinder is steady and symmetric with respect to the wake centerline at $\mathrm{Re} = 40$; however, for the flexible cantilever cylinder, the wake is unstable at the same Re. To

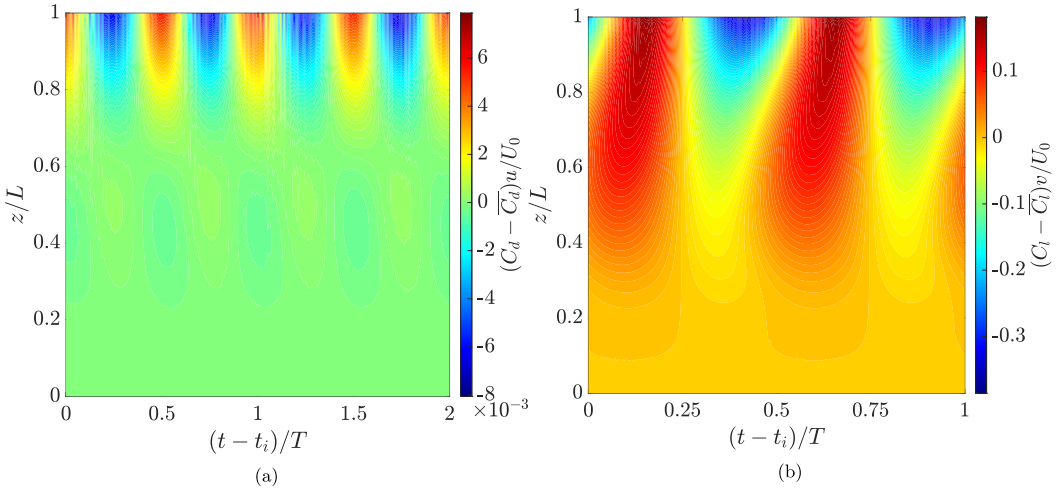

FIG. 11. Instantaneous power transfer between the flexible cantilever cylinder and fluid flow in the (a) streamwise and (b) transverse directions. The cylinder is an energy sink (source) in regions with positive (negative) values. The results are gathered at $\mathrm{Re} = 40$, $m^* = 1$, and $U^* = 7$ over one period of the cylinder motion, i.e., $T = 1/f_{\mathrm{n}}$. t_i is the intial sampling time.

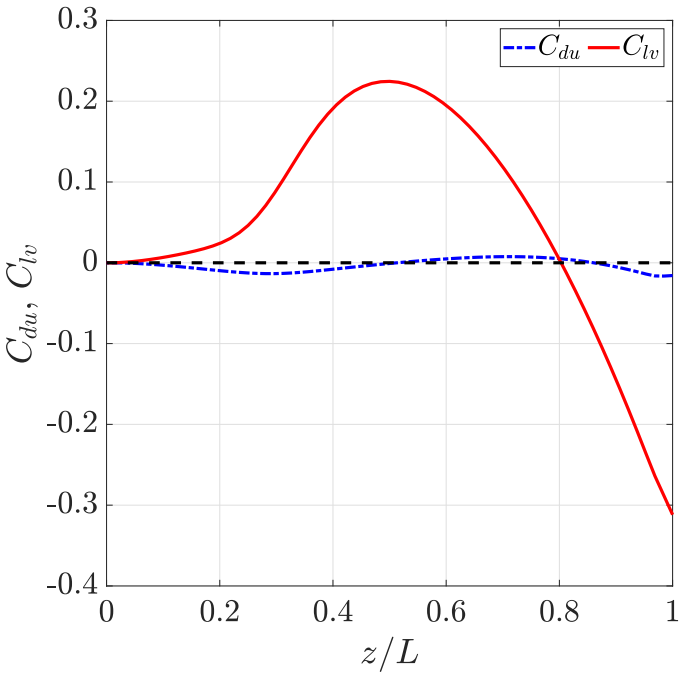

FIG. 12. Distribution of the hydrodynamic coefficients along the cylinder span at Re = 40, $m^* = 1$, and $U^* = 7$.

illustrate, we have examined the z-vorticity (ω_z) contours at different cross sections of the flexible cantilever cylinder. As shown in Fig. 14, the wake of the cylinder is steady at $z/L = 0$ where it is connected to the fixed support; however, by approaching the free end of the cylinder, the flow starts to become unstable, and periodic vortex-shedding patterns are observed downstream. This finding suggests that there is a connection between the cylinder motion and wake stability at laminar subcritical Re.

The z-vorticity isosurfaces of the three-dimensional wake structures at Re = 30 and $m^* = 1$ are given in Fig. 15 for $U^* = 3, 7$, and 15. For the given Re and m^*, $U^* = 3, 7$, and 15 represent the pre-lock-in, lock-in, and post-lock-in regimes, respectively. We find that the flow field in the wake of the flexible cantilever cylinder is steady at $U^* = 3$ (pre-lock-in) and $U^* = 15$ (post-lock-in); however, an unsteady wake is observed at $U^* = 7$ (see Fig. 15). The phase diagram of the wake stability as a function of Re and U^* at $m^* = 1$ is given in Fig. 16. According to the phase diagram, given in Fig. 16, we find that at Re = 20, the flow field is steady for all U^* values; however, as Re increases, the wake is found to become unstable for a particular range of U^*. The flow field in the wake of the flexible cantilever cylinder is shown to lose its stability at Re = 22 for $U^* \in [7, 9]$. This range is shown to become wider for higher Re. For example, at Re = 30, this range is between $U^* \in [6, 13]$, increasing to $U^* \in [6, 19]$ at Re = 40. One thing to note here is that there is a critical $U^* \in [6, 7]$, which marks the initiation of the wake unsteadiness for $22 \leqslant \mathrm{Re} \leqslant 40$. This critical U^* also marks the lower bound of the lock-in regime, as discussed in Sec. III A. According to these findings, we conclude that the range of the wake unsteadiness at laminar subcritical Re is closely correlated with the range of the lock-in regime. The wake structures around the flexible cantilever cylinder at Re = 40 and $m^* = 1$ are given in Fig. 17 for $5 \leqslant U^* \leqslant 14$. We observe that in the pre-lock-in regime at $U^* = 5$, a steady wake flow is present behind the cylinder; however, for $U^* \geqslant 6$, the wake is found to become unstable, with two alternate vortices being shed from the cylinder wake in each cycle (see Fig. 17). In addition, the wake structures in the vicinity of the cylinder's

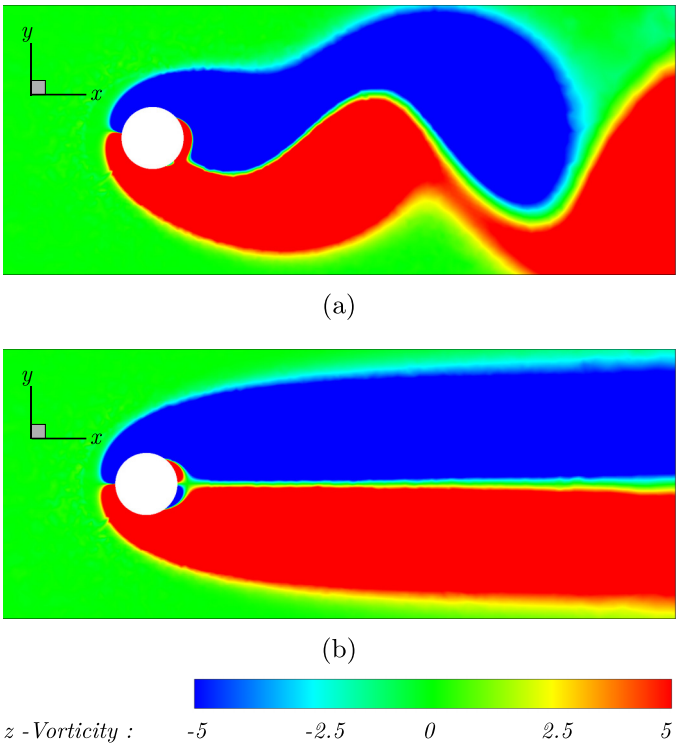

FIG. 13. Comparison of the z-vorticity contour for (a) the flexible cantilever cylinder and (b) its stationary rigid counterpart at $z/L = 0.5$, Re $= 40$, $m^* = 1$, $U^* = 7$, and $tU_0/D = 200$.

fixed end are found to be steady and symmetric for all values of U^*. This observation suggests that the vorticity patterns vary across the cylinder span. In addition, the streamwise vortices, which start to appear at Re ≈ 180 [44] for the flow around a stationary rigid cylinder, are not observed over the span of the flexible cantilever cylinder for the range of studied Re.

With these findings, the two essential requirements for the wake unsteadiness at laminar subcritical Re are (1) the flow needs to have sufficiently large inertia to overcome the viscous damping and (2) the system parameters need to be in the lock-in range to sustain the unsteadiness in the wake. In the following, we discuss the relationship between the cylinder motion and stability of the wake in detail.

C. Relationship between the cylinder motion and wake unsteadiness

In this subsection we discuss the relationship between the cylinder motion and stability of the wake at laminar subcritical Re. We suggest a combined VIV-galloping-type instability as the possible cause of the wake unsteadiness for Re $<$ Re$_{cr}$. Galloping is a velocity-dependent and damping-controlled fluid-structure instability, which is generally observed in geometrically asymmetric structures [45]. Although the flow field around an asymmetric structure is uniform in magnitude and direction, cross-flow movements of the asymmetric body alter the magnitude and direction of the incident flow with respect to the body coordinate system. This change, in turn, alters the fluid forces acting on the body and could trigger galloping instability. A deviation from symmetric cross section in transmission lines due to ice formation [46] or in marine cables due to marine organisms [47] are some examples of the galloping instability in engineering structures. Galloping is known to cause large-amplitude sustained oscillations in elastically mounted and

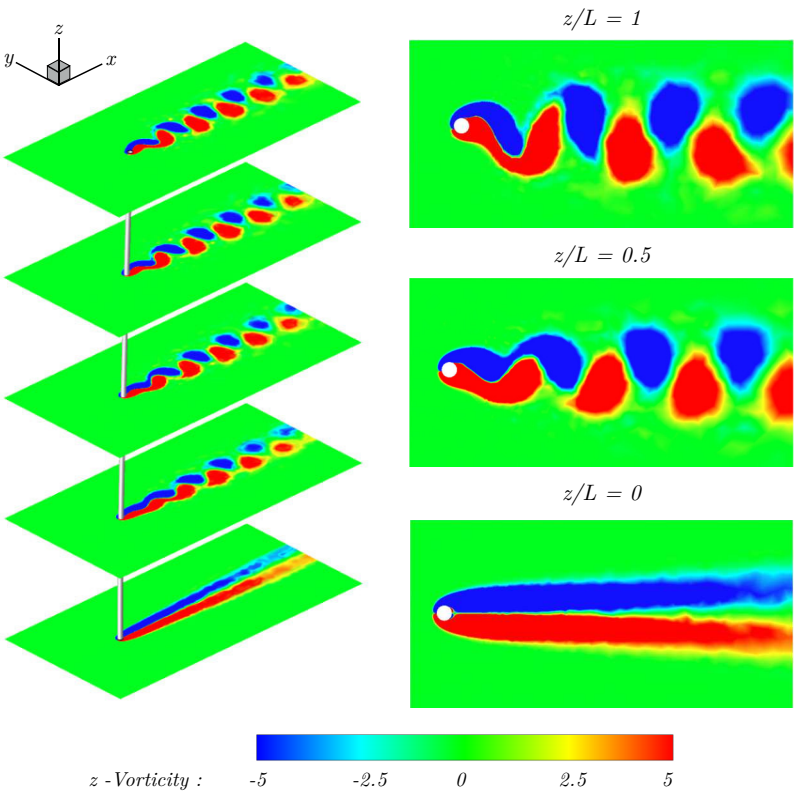

FIG. 14. Isometric view of the z-plane slices of the z-vorticity contour for the flexible cantilever cylinder at Re $= 40$, $m^* = 1$, and $U^* = 7$, with the slices at $z/L = 1$, 0.5, and 0 shown in the right-hand side.

flexible structures [45]. In contrast to vortex-induced vibrations, galloping instability is induced by a relative body motion rather than the unsteady fluctuations of the flow field; hence it can occur even for steady attached flows. When the transverse force acting on a flexible or elastically mounted body increases in the direction of motion, it adds movement to the body, and the body will displace further until the opposing stiffness or damping overcomes the movements, or the transverse force decreases when the movement is increased.

For the flexible cantilever cylinder interacting with fluid flow, the body is free to deform in the streamwise and transverse directions. Although displacements in the streamwise direction do not contribute to the stability of the wake [48,49], relative movements in the transverse direction break the wake symmetry, altering the fluid forces acting on the cylinder. This symmetry breakdown, in turn, induces galloping-type instability by creating negative damping in the combined fluid-structure system. The low-speed galloping-type instability, together with the frequency lock-in, is most arguably the mechanism that leads to sustained unsteadiness in the wake and large-amplitude vibrations of the flexible cantilever cylinder at laminar subcritical Re.

To better understand the relationship between the cylinder motion and stability of the wake at laminar subcritical Re, we have provided the z-vorticity contours at the midsection of the cylinder at Re $= 40$, $m^* = 1$, and $U^* = 7$ in Fig. 18. As seen in Fig. 18, the wake region is steady and symmetric at $tU_0/D = 60$; however, for $tU_0/D \in [65, 75]$, the relative motion of the cylinder cross section in the transverse direction, breaks down the wake symmetry. This symmetry breakdown, in turn, exerts a transverse load that further increases the cylinder motion. Finally, the coupling

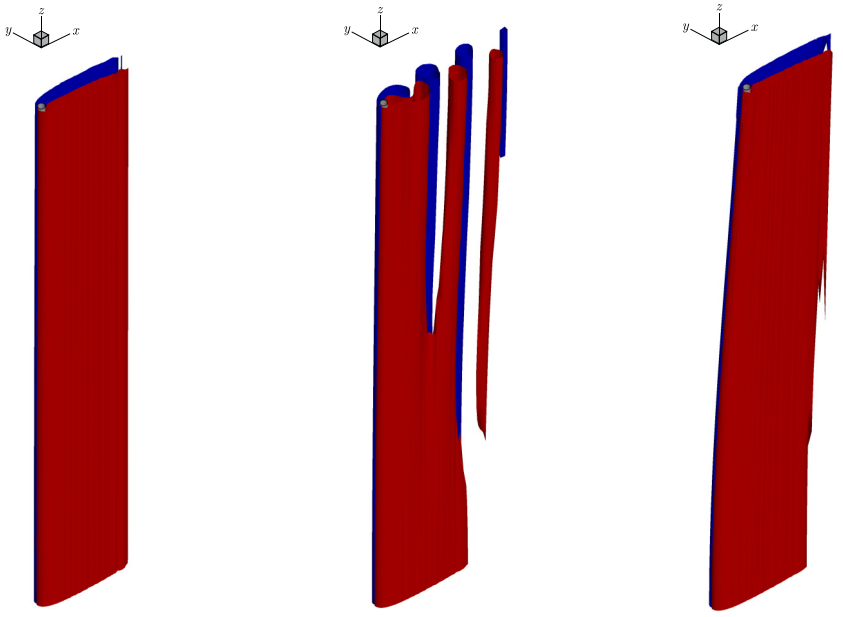

(a) $U^* = 3$ (b) $U^* = 7$ (c) $U^* = 15$

FIG. 15. Wake structures visualized by the normalized z-vorticity isosurfaces ($\omega_z D/U_0 = -0.224, 0.224$) for the flexible cantilever cylinder at Re $= 30$ and $m^* = 1$. Red (blue) indicates regions of positive (negative) vortices.

between the unsteady wake and the cylinder movements leads to large-amplitude vibrations for $tU_0/D \geqslant 80$. In the following, we investigate the effect of mass ratio m^* on the dynamics of the flexible cantilever cylinder and further examine the wake structures in the lock-in regime.

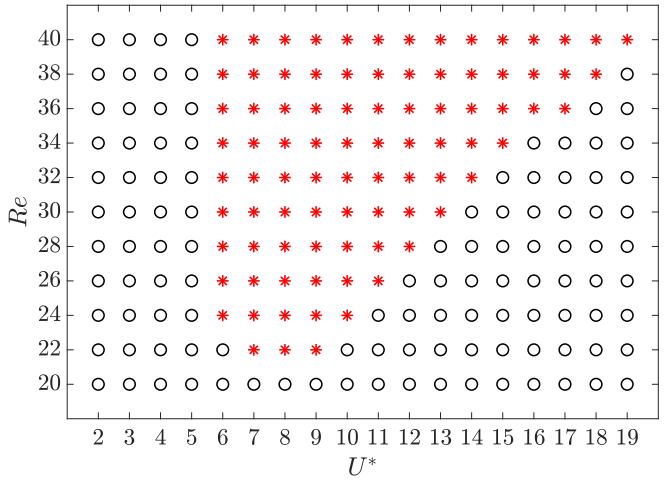

FIG. 16. Phase diagram of the wake stability as a function of Re and U^* at $m^* = 1$. Here $\circ$ denotes a steady wake, while $*$ represents an unsteady wake behind the flexible cantilever cylinder.

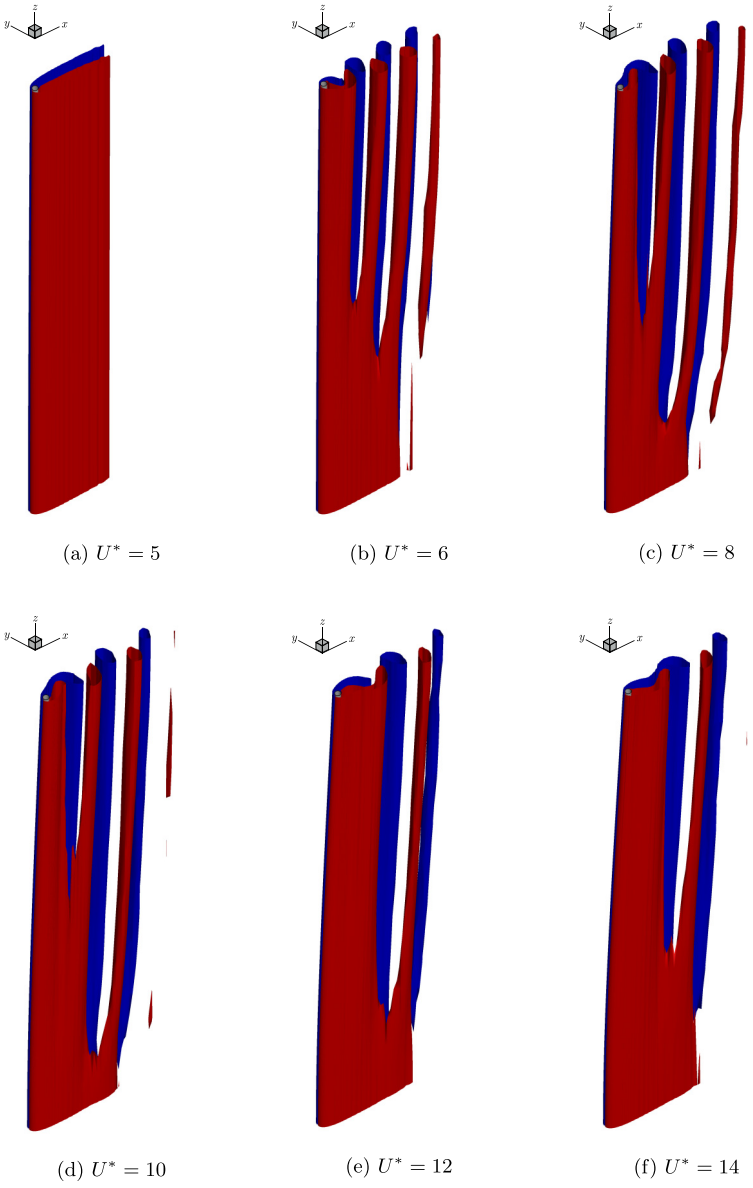

(a) $U^* = 5$ (b) $U^* = 6$ (c) $U^* = 8$

(d) $U^* = 10$ (e) $U^* = 12$ (f) $U^* = 14$

FIG. 17. Wake structures visualized by the normalized z-vorticity isosurfaces ($\omega_z D/U_0 = -0.224, 0.224$) for the flexible cantilever cylinder at Re $= 40$ and $m^* = 1$. Red (blue) indicates regions of positive (negative) vortices.

D. Effect of mass ratio

We next investigate the response of the cylinder at four different mass ratios, namely, $m^* =$ 1, 10, 100, and 1000 at Re $= 40$ for $U^* \in [2, 19]$. The results for the rms value of the dimensionless transverse vibration amplitude A_y^{rms}/D with respect to U^* are given in Fig. 19. For the range of studied mass ratios, we find that the cylinder stays at its steady deflected position, i.e., $A_y^{rms}/D = 0$, for $U^* \leqslant 5$. This steady response is present for the whole range of U^* at $m^* = 1000$. However, a discrete change in the dynamic response of the cylinder is observed for higher U^* values at

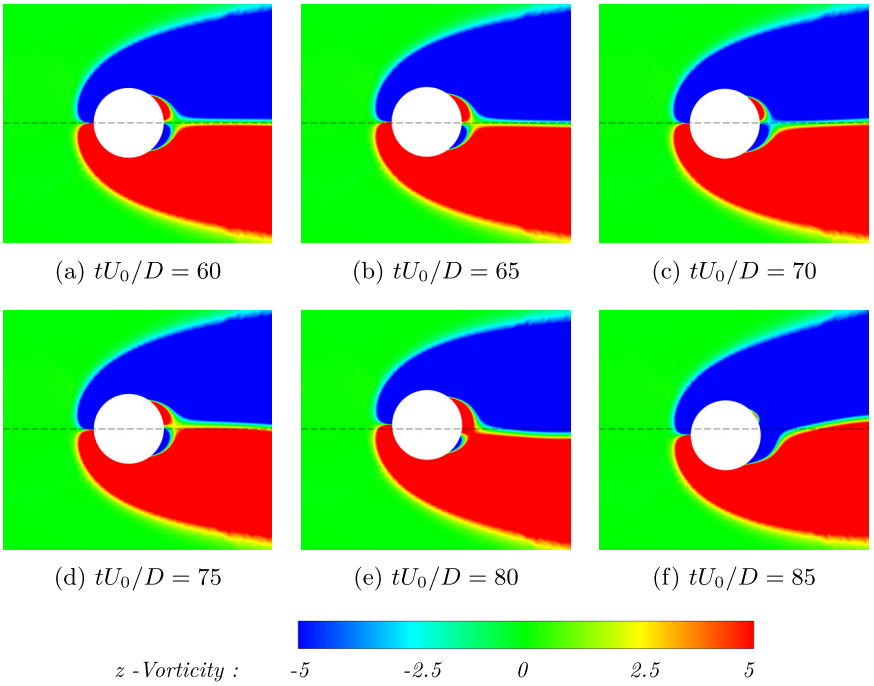

FIG. 18. Z-plane slices of the z-vorticity contour for the flexible cantilever cylinder at Re $= 40$, $m^* = 1$, and $U^* = 7$ in the time window $tU_0/D \in [60, 85]$. The slices are gathered at $z/L = 0.5$.

$m^* = 1$, 10, and 100. A sudden jump in the amplitude response of the cylinder is observed at $U^* = 6$, 7, and 8 for mass ratios $m^* = 1$, 10, and 100, respectively. As shown in Fig. 19, the peak of A_y^{rms}/D is at $U^* = 7$ for $m^* = 1$ and 10, and at $U^* = 8$ for $m^* = 100$. The maximum value of

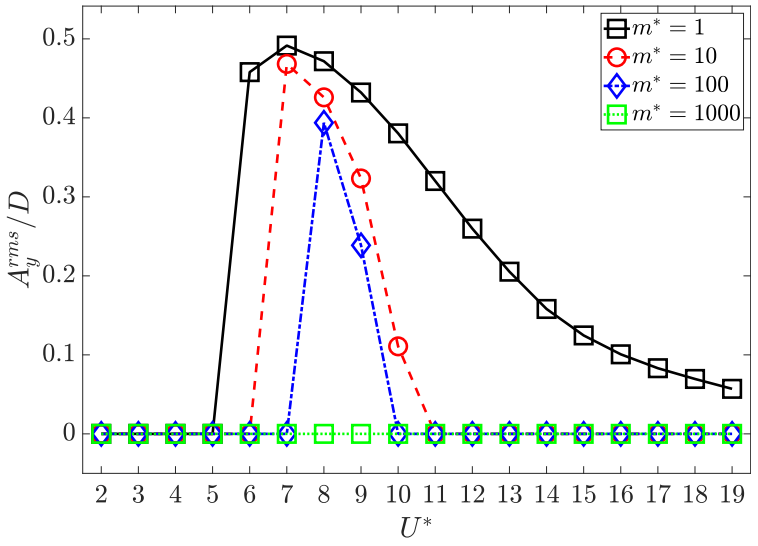

FIG. 19. Root-mean-square value of the dimensionless transverse vibration amplitude A_y^{rms}/D at $z/L = 1$ as a function of U^* at Re $= 40$ for $m^* = 1$, 10, 100, and 1000.

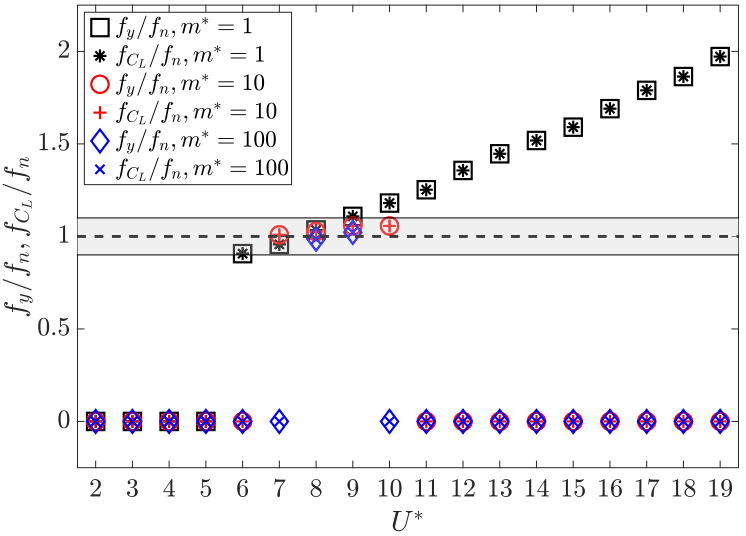

FIG. 20. Variations of the dimensionless transverse vibration frequency f_y/f_n, probed at $z/L = 1$, and the dimensionless lift coefficient frequency f_{C_L}/f_n with respect to U^*. The results are gathered at $\mathrm{Re} = 40$ for $m^* = 1$, 10, and 100.

A_y^{rms}/D is found to be approximately 0.49, 0.47, and 0.39 at $m^* = 1$, 10, and 100, respectively. By further increasing U^*, a gradual decrease in the value of A_y^{rms}/D is observed at $m^* = 1$; however, for $m^* = 10$ and 100, this value is shown to decrease rapidly for $U^* > 8$. For $U^* \geqslant 11$ at $m^* = 10$ and $U^* \geqslant 10$ at $m^* = 100$, the cylinder is shown to remain in its steady deflected position.

Figure 20 shows the frequency response of the system in terms of the dimensionless transverse vibration frequency f_y/f_n and the dimensionless lift coefficient frequency f_{C_L}/f_n at $\mathrm{Re} = 40$ for $m^* = 1$, 10, and 100. We show that for all three mass ratios, there is a frequency match between the frequency of the transverse vibrations f_y, frequency of the lift coefficient f_{C_L}, and the first-mode natural frequency of the cylinder f_n for a specific range of U^*. This range is within $U^* \in [8, 9]$ at $m^* = 100$ and within $U^* \in [7, 10]$ at $m^* = 10$. At $m^* = 1$, the lock-in regime is within $U^* \in [6, 9]$; however, the cylinder is shown to oscillate in frequencies higher than its first-mode natural frequency at larger U^* values. Based on our findings, the range of the lock-in regime becomes narrower as m^* is increased. This behavior is due to stronger inertial coupling and added mass effects at lower mass ratios. It should be noted that for Reynolds numbers beyond $\mathrm{Re}_{cr} \approx 45$, interactions between the unsteady wake and the cylinder motion could lead to sustained vibrations in the flexible cantilever cylinder at mass ratios of $O(100–1000)$, which are not examined in our current work. A qualitative representation of the cylinder motion trajectories at $z/L = 1$ and $\mathrm{Re} = 40$ with respect to U^* is given in Fig. 21 for $m^* = 1$, 10, and 100. It is shown that as m^* is increased, the motion trajectory of the cylinder in the lock-in regime shifts from a figure-eight-shape trajectory at $m^* = 1$ to a dominated motion in the transverse direction at $m^* = 100$. To examine the effect of mass ratio on the wake structures behind the flexible cantilever cylinder, we have provided the z-vorticity isosurfaces around the cylinder at $\mathrm{Re} = 40$ and $U^* = 8$ for $m^* = 1$, 10, and 100 in Fig. 22. We observe that for all three m^*, two alternate vortices are shed from the cylinder wake in each cycle. Thus, the mass ratio m^* does not affect the vortex-shedding patterns behind the flexible cantilever cylinder in the lock-in regime.

E. Connection to whisker dynamics

To help understand the role of fluid-structure interactions in the problem of sensing through whiskers, we relate our results for the flexible cantilever cylinder, as a canonical model of a whisker,

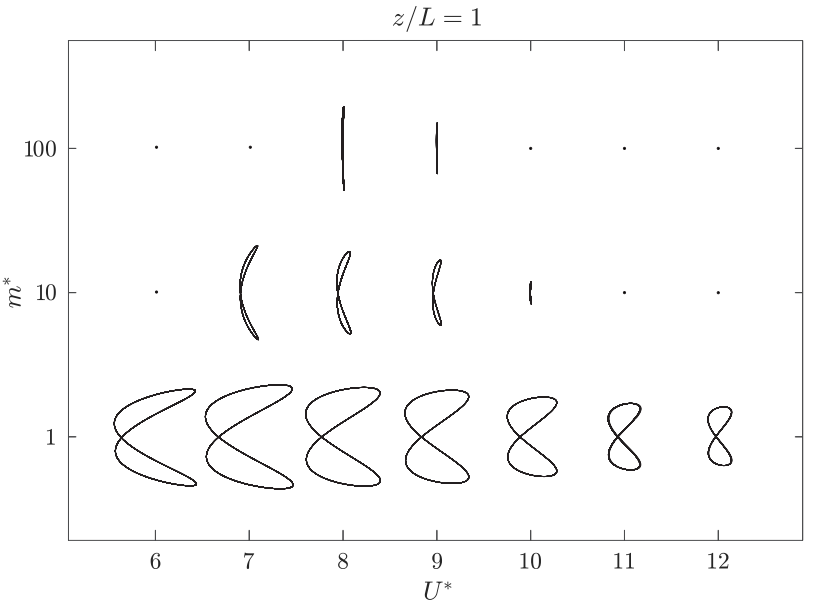

FIG. 21. Motion trajectory of the flexible cantilever cylinder with respect to U^* at $z/L = 1$ and $\mathrm{Re} = 40$ for $m^* = 1$, 10, and 100. The dot symbol $(\cdot)$ represents a steady response.

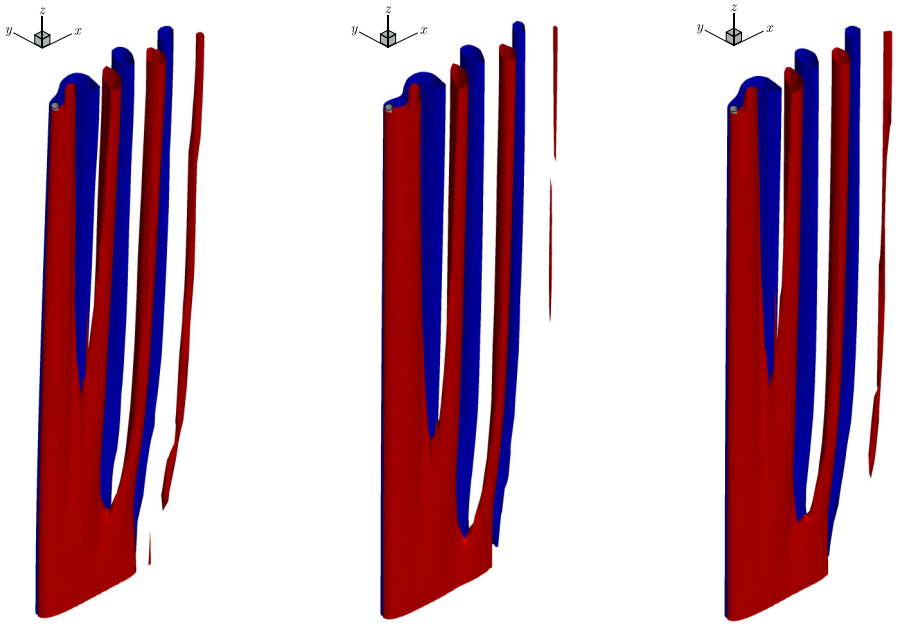

(a) $m^* = 1$ (b) $m^* = 10$ (c) $m^* = 100$

FIG. 22. Wake structures visualized by the normalized z-vorticity isosurfaces ($\omega_z D/U_0 = -0.224, 0.224$) for the flexible cantilever cylinder at $\mathrm{Re} = 40$ and $U^* = 8$. Red (blue) indicates regions of positive (negative) vortices.

to real-world observations in rats' and seals' whiskers. According to a recent experimental study, an isolated rat whisker in uniform fluid flow experiences sustained vibrations for Re $<$ 50 [29]. The vibration frequencies of a rat's whisker in fluid flow have been found to match the resonance frequencies of the whisker, indicating the presence of the lock-in phenomenon [29]. Within the range of studied parameters for the flexible cantilever cylinder, our results for $m^* = 1000$ at Re $= 40$ could be used to interpret the dynamics of a rat's whisker at laminar subcritical Re. According to our findings, a rat's whisker interacting with the uniform flow at $m^* = 1000$ is unlikely to experience flow-induced vibrations for $U^* \in [2, 19]$. This is mainly due to weak inertial coupling and added mass effects at this m^*. For a rat's whisker in uniform flow, we anticipate the presence of vortex-induced vibrations at higher modes of vibrations for reduced velocities of $O(100)$.

For the case of a seal whisker in flowing water, we characterize the oscillations as a VIV-dominant mechanism due to interactions between the whisker and surrounding flow in the lock-in regime. Our results for the dynamic response of the flexible cantilever cylinder at $m^* = 1$ could be used to interpret the dynamics of a seal whisker in low-speed laminar water flows. Under similar conditions, a seal whisker is anticipated to have lower vibration amplitudes compared to the vibration amplitude of the flexible cantilever cylinder. This characteristic is mainly due to the seal whisker's undulated geometry that helps reduce fluid forces during VIVs [33,34]. There is a need for further investigation on how hydrodynamic disturbances, i.e., vortex trail, interact with the whisker array and how weak hydrodynamic signals are transmitted to the whisker base for the vortex-sensing abilities.

IV. CONCLUSIONS

In this paper, we have investigated the fluid-structure interaction of a flexible cantilever cylinder at laminar subcritical Re. Through numerical simulations, we assessed the dynamic response of the cylinder as a function of reduced velocity U^*, for Reynolds numbers between $20 \leqslant \text{Re} \leqslant 40$ and mass ratios between $1 \leqslant m^* \leqslant 1000$. We found that for Re $= 20$, the flexible cantilever cylinder remains in its steady deflected position for the whole range of studied U^* and m^*. However, for $22 \leqslant \text{Re} \leqslant 40$, the cylinder was shown to experience sustained oscillations when certain conditions were satisfied. We showed that the frequency of the transverse vibrations matches the frequency of the periodic lift force during the oscillations. Moreover, these two frequencies were found to be approximately equal to the first-mode natural frequency of the cylinder for a particular range of U^*. This specific range, known as the lock-in regime, was shown to be strongly dependent on the Reynolds number Re and mass ratio m^*; at laminar subcritical Re, the range of the lock-in regime was shown to decrease by increasing m^* and increase by increasing Re. Finally, we identified two requirements for the wake unsteadiness at laminar subcritical Re: (1) the flow should possess sufficiently large inertia to overcome the viscous damping effects and (2) the system parameters should be in the lock-in range. When these two conditions are satisfied, the cylinder experiences a combined VIV-galloping type instability, leading to sustained large-amplitude vibrations at laminar subcritical Re. The presented systematic analysis can help improve our understanding of the lock-in mechanism in flexible cantilever structures. Further research is required towards a parametric investigation of the dynamic response of the cylinder at reduced velocities of $O(100)$, where potential multi-lock-in phenomenon and flutter-type instabilities could be present. In addition, the effects of structural nonlinearities should be considered from a practical viewpoint for different flow incidence and a broader range of Re and U^* to fully understand the dynamic instabilities of the coupled system.

ACKNOWLEDGMENTS

The authors would like to acknowledge the Natural Sciences and Engineering Research Council of Canada for funding the project. The research was enabled in part through

computational resources and services provided by WestGrid, Compute Canada, and the Advanced Research Computing facility at the University of British Columbia.

[1] Y. Z. Law and R. K. Jaiman, Wake stabilization mechanism of low-drag suppression devices for vortex-induced vibration, J. Fluids Struct. **70**, 428 (2017).
[2] A. Chizfahm and R. Jaiman, Data-driven stability analysis and near-wake jet control for the vortex-induced vibration of a sphere, Phys. Fluids **33**, 044104 (2021).
[3] S. Dong, G. S. Triantafyllou, and G. E. Karniadakis, Elimination of Vortex Streets in Bluff-Body Flows, Phys. Rev. Lett. **100**, 204501 (2008).
[4] Y. Xia, S. Michelin, and O. Doaré, Fluid-Solid-Electric Lock-In of Energy-Harvesting Piezoelectric Flags, Phys. Rev. Applied **3**, 014009 (2015).
[5] A. Chizfahm, E. A. Yazdi, and M. Eghtesad, Dynamic modeling of vortex induced vibration wind turbines, Renew. Energy **121**, 632 (2018).
[6] W. B. Hobbs and D. L. Hu, Tree-inspired piezoelectric energy harvesting, J. Fluids Struct. **28**, 103 (2012).
[7] Y. J. Lee, Y. Qi, G. Zhou, and K. B. Lua, Vortex-induced vibration wind energy harvesting by piezoelectric MEMS device in formation, Sci. Rep. **9**, 20404 (2019).
[8] P. S. Gurugubelli and R. K. Jaiman, Self-induced flapping dynamics of a flexible inverted foil in a uniform flow, J. Fluid Mech. **781**, 657 (2015).
[9] J. Z. Gul, K. Y. Su, and K. H. Choi, Fully 3D printed multi-material soft bio-inspired whisker sensor for underwater-induced vortex detection, Soft Robotics **5**, 122 (2018).
[10] M. Scharff, P. Schorr, T. Becker, C. Resagk, J. H. A. Miranda, and C. Behn, An artificial vibrissa-like sensor for detection of flows, Sensors (Switzerland) **19**, 3892 (2019).
[11] R. D. Blevins, *Flow-Induced Vibration* (Van Nostrand Reinhold, New York, 1990).
[12] A. Khalak and C. H. K. Williamson, Motions, forces and mode transitions in vortex-induced vibrations at low mass-damping, J. Fluids Struct. **13**, 813 (1999).
[13] T. Sarpkaya, Vortex-induced oscillations: A selective review, J. Appl. Mech. **46**, 241 (1979).
[14] C. H. K. Williamson and R. Govardhan, Vortex-induced vibrations, Annu. Rev. Fluid Mech. **36**, 413 (2004).
[15] P. W. Bearman, Circular cylinder wakes and vortex-induced vibrations, J. Fluids Struct. **27**, 648 (2011).
[16] N. Jauvtis and C. H. K. Williamson, The effect of two degrees of freedom on vortex-induced vibration at low mass and damping, J. Fluid Mech. **509**, 23 (2004).
[17] R. N. Govardhan and C. H. K. Williamson, Defining the 'modified Griffin plot' in vortex-induced vibration: Revealing the effect of Reynolds number using controlled damping, J. Fluid Mech. **561**, 147 (2006).
[18] C. H. Williamson and R. Govardhan, A brief review of recent results in vortex-induced vibrations, J. Wind Eng. Ind. Aerodyn. **96**, 713 (2008).
[19] T. Sarpkaya, A critical review of the intrinsic nature of vortex-induced vibrations, J. Fluids Struct. **19**, 389 (2004).
[20] R. H. J. Willden and J. M. R. Graham, Bluff body wakes and vortex-induced vibrations multi-modal vortex-induced vibrations of a vertical riser pipe subject to a uniform current profile, Eur. J. Mech. B Fluids **23**, 209 (2004).
[21] A. D. Trim, H. Braaten, H. Lie, and M. Tognarelli, Experimental investigation of vortex-induced vibration of long marine risers, J. Fluids Struct. **21**, 335 (2005).
[22] J. K. Vandiver, V. Jaiswal, and V. Jhingran, Insights on vortex-induced, traveling waves on long risers, J. Fluids Struct. **25**, 641 (2009).
[23] R. Bourguet, G. E. Karniadakis, and M. S. Triantafyllou, Vortex-induced vibrations of a long flexible cylinder in shear flow, J. Fluid Mech. **677**, 342 (2011).
[24] V. Joshi and R. K. Jaiman, A variationally bounded scheme for delayed detached eddy simulation: Application to vortex-induced vibration of offshore riser, Comput. Fluids **157**, 84 (2017).

[25] G. R. Franzini, C. P. Pesce, R. T. Gonçalves, A. L. C. Fujarra, and P. Mendes, An experimental investigation on concomitant vortex-induced vibration and axial top-motion excitation with a long flexible cylinder in vertical configuration, Ocean Eng. **156**, 596 (2018).
[26] G. Baarholm, C. Larsen, and H. Lie, On fatigue damage accumulation from in-line and cross-flow vortex-induced vibrations on risers, J. Fluids Struct. **22**, 109 (2006).
[27] J. R. Chaplin, P. W. Bearman, F. J. Huera Huarte, and R. J. Pattenden, Laboratory measurements of vortex-induced vibrations of a vertical tension riser in a stepped current, J. Fluids Struct. **21**, 3 (2005).
[28] J. K. Shang, H. A. Stone, and A. J. Smits, Vortex and structural dynamics of a flexible cylinder in cross-flow, Phys. Fluids **26**, (2014).
[29] Y. S. W. Yu, N. E. Bush, and M. J. Z. Hartmann, Whisker vibrations and the activity of trigeminal primary afferents in response to airflow, J. Neurosci. **39**, 5881 (2019).
[30] Y. S. W. Yu, M. M. Graff, and M. J. Z. Hartmann, Mechanical responses of rat vibrissae to airflow, J. Exp. Biol. **219**, 937 (2016).
[31] Y. S. W. Yu, M. M. Graff, C. S. Bresee, Y. B. Man, and M. J. Z. Hartmann, Whiskers aid anemotaxis in rats, Sci. Adv. **2**, 1 (2016).
[32] G. Dehnhardt, B. Mauck, W. Hanke, and H. Bleckmann, Hydrodynamic trail-following in harbor seals (*Phoca vitulina*), Science **293**, 102 (2001).
[33] W. Hanke, M. Witte, L. Miersch, M. Brede, J. Oeffnet, M. Michael, F. Hanke, A. Leder, and G. Dehnhardt, Harbor seal vibrissa morphology suppresses vortex-induced vibrations, J. Exp. Biol. **213**, 2665 (2010).
[34] H. R. Beem and M. Triantafyllou, Wake-induced 'slaloming' response explains exquisite sensitivity of seal whisker-like sensors, J. Fluid Mech. **783**, 306 (2015).
[35] C. T. Murphy, C. Reichmuth, W. C. Eberhardt, B. H. Calhoun, and D. A. Mann, Seal whiskers vibrate over broad frequencies during hydrodynamic tracking, Sci. Rep. **7**, 8350 (2017).
[36] M. Muthuramalingam and C. Bruecker, Seal and sea lion whiskers detect slips of vortices similar as rats sense textures, Sci. Rep. **9**, 12808 (2019).
[37] D. Park and K. S. Yang, Flow instabilities in the wake of a rounded square cylinder, J. Fluid Mech. **793**, 915 (2016).
[38] W. Yao and R. K. Jaiman, Model reduction and mechanism for the vortex-induced vibrations of bluff bodies, J. Fluid Mech. **827**, 357 (2017).
[39] T. J. R. Hughes, W. K. Liu, and T. K. Zimmermann, Lagrangian-Eulerian finite element formulation for incompressible viscous flows, Comput. Methods Appl. Mech. Eng. **29**, 329 (1981).
[40] R. D. Blevins, *Formulas for Dynamics, Acoustics and Vibration* (Wiley, New York, 2016).
[41] R. K. Jaiman, M. Z. Guan, and T. P. Miyanawala, Partitioned iterative and dynamic subgrid-scale methods for freely vibrating square-section structures at subcritical Reynolds number, Comput. Fluids **133**, 68 (2016).
[42] R. K. Jaiman, N. R. Pillalamarri, and M. Z. Guan, A stable second-order partitioned iterative scheme for freely vibrating low-mass bluff bodies in a uniform flow, Comput. Methods Appl. Mech. Eng. **301**, 187 (2016).
[43] R. D. Henderson, Details of the drag curve near the onset of vortex shedding, Phys. Fluids **7**, 2102 (1995).
[44] C. H. Williamson, Mode A secondary instability in wake transition, Phys. Fluids **8**, 1680 (1996).
[45] D. J. P. Hartog, *Mechanical Vibrations* (Dover Publications, New York, 1985).
[46] P. V. Dyke, D. Havard, and A. Lanevill, Effect of ice and snow on the dynamics of transmission line conductors, in *Atmospheric Icing of Power Networks*, edited by M. Farzaneh, 1st ed. (Springer Netherlands, Dordrecht, 2008), pp. 171–228.
[47] A. Simpson, Determination of the natural frequencies of multiconductor overhead transmission lines, J. Sound Vib. **20**, 417 (1972).
[48] S. Tang and N. Aubry, On the symmetry breaking instability leading to vortex shedding, Phys. Fluids **9**, 2550 (1997).
[49] G. L. Vasconcelos, M. N. Moura, and A. M. J. Schakel, Vortex motion around a circular cylinder, Phys. Fluids **23**, 123601 (2011).